



Access provided by University of Szeged



CRITICAL REVIEW | ARTICLES IN PRESS, 101042

Magnetic Resonance Imaging–Based Delineation of Organs at Risk in the Head and Neck Region

Viktor R. Paczona, MD   • Marta E. Capala, MD, PhD • Borbála Deák-Karancsi, MD • ...

Adrienne Cserhádi, MD • Florian Wiesinger, PhD • Katalin Hideghéty, MD, PhD • Show all authors

[Open Access](#) • Published: July 30, 2022 • DOI: <https://doi.org/10.1016/j.adro.2022.101042>

 PlumX Metrics

Abstract

Purpose

The aim of this article is to establish a comprehensive contouring guideline for treatment planning using only magnetic resonance images through an up-to-date set of organs at risk (OARs), recommended organ boundaries, and relevant suggestions for the magnetic resonance imaging (MRI)–based delineation of OARs in the head and neck (H&N) region.

Methods and Materials

After a detailed review of the literature, MRI data were collected from the H&N region of healthy volunteers. OARs were delineated in the axial, coronal, and sagittal planes on T2-weighted sequences. Every contour defined was revised by 4 radiation oncologists and subsequently by 2 independent senior experts (H&N radiation oncologist and radiologist). After revision, the final res were presented to the consortium partners.



Results

A definitive consensus was reached after multi-institutional review. On that basis, we provided a detailed anatomic and functional description and specific MRI characteristics of the OARs.

Conclusions



MRI may lead to increased accuracy in terms of organ boundaries and analysis of dose-dependent sequelae for an adequate definition of normal tissue complication probability.

Introduction

Accurate organ-at-risk (OAR) delineation in the era of precision radiation therapy (RT) is essential for the irradiation of head and neck (H&N) cancer. Both postoperative and definitive organ-preserving RT with or without chemotherapy are widely applied in the complex management of this disease. Although RT is highly effective in the treatment of cancer, a substantial rate of serious acute side effects and often severe, treatment-related late toxicities occur. Acute mucositis during dose delivery, as well as late functional damages of healthy organs, may lead to xerostomia and swallowing difficulties, significantly deteriorating the quality of life of patients. A consistent definition and delineation of OARs using highly selective, conformal plans is vital to spare normal structures.

Both traditionally and at the present time, the generally used imaging method for contouring purposes is computed tomography (CT). A consensus guideline¹ was published in 2015 on CT-based OAR delineation for the H&N region. However, the hegemony of CT is challenged by newly emerged, advanced methods that provide detailed images with far superior soft-tissue resolution compared with CT (magnetic resonance imaging [MRI]).^{2,3} MRI-only treatment planning has several clinical advantages, such as the avoidance of multiple imaging processes and exposure to ionizing radiation during imaging. The latter has a greater relevance if repeated imaging is applied for replanning purposes during adaptive RT.

However, MRI-only based contouring has a number of drawbacks as well. Due to the more complex physical background, selecting and interpreting adequate sequences require more experience. Moreover, getting to know the specific MRI characteristics of the given OARs may take a longer time and more practice. In the future, owing to automated OAR delineation, this learning process will become needless, and errors due to human mistakes will be less likely to occur. With the availability of such modalities, the need for a large number of accur

contours in the H&N region, including subunits of larger organs and organelles, can be satisfied. Although MRI has long been used for tumor delineation, its implication in OAR contouring remains a question of debate.^{4, 5, 6}

Since 2015, many studies have been published, focusing on new potential OARs in the anatomic region at hand. As a result of this process, numerous different sets of OARs coexist, in some



images through an up-to-date set of OARs, recommended organ boundaries, and relevant suggestions of the MRI-based delineation of OARs.

Methods and Materials

The ongoing project, XXXX, aims to develop a software that can provide automatic OAR contours on magnetic resonance images.⁷ The first phase of the development required numerous precise, manually contoured expert cases. During the project, the need emerged for a definition of MRI acquisition techniques and delineation of OARs in the H&N region on magnetic resonance images. To that aim, the technical details of MRI acquisition for treatment planning, reasonably required MRI sequences, and an up-to-date set of OARs were defined, relying on the latest existing guidelines.^{1,8, 9, 10, 11, 12, 13, 14} The method comprised of a systematic review of the latest publications and discussions for a consensus in divergent points by representatives of the participating institutions.

The next step was MRI data collection from the H&N region of 7 healthy volunteers in a diagnostic setting (supine position, dedicated H&N coil; [Table 1](#)). The OARs were delineated using the ECLIPSE treatment planning system (Varian Medical Systems, version 13.6) in the axial, coronal, and sagittal planes on T2-weighted sequences. Every contour defined was revised by 4 radiation oncologists and subsequently by 2 independent senior experts (H&N radiation oncologist and radiologist). After this 2-step revision, the final structures were presented to the consortium partners in Rotterdam, The Netherlands. A definitive consensus was reached after multi-institutional review. To visualize our findings and suggestions, we compiled an atlas containing an expert case (Supplementary Materials). MRI for OAR delineation was based on 2- and 3-dimensional, T2-weighted, fast-spin echo (FSE) sequences with sufficient geometric coverage to include all relevant OARs (ie, top of head to middle of neck). More specifically, the T2 FSE sequences included 2-dimensional fast-recovery FSE, 2-dimensional PROPELLER, and 3-dimensional CUBE. Detailed sequence parameters are outlined in [Table 1](#).



Table 1 Scan parameters for 3 T2-weighted sequences used for organ-at-risk delineation

	2-Dimensional T2 fast- spin-echo (FSE)	2-Dimensional T2 PROPELLER	3-Dimensional T2 GRE
Magnetic resonance scanner model	GE DISCOVERY MR750w	GE SIGNA Artist	GE SIGNA Artist
Radiofrequency receive coil array	AIR RT Head&Neck	GEM Head&Neck	GEM Head&Neck
Main magnetic field strength, T	3	1.5	1.5
Bandwidth, kHz*	62.5	83.3	125
Repetition time, ms	11866	7624	2002
Echo time, ms	99.3	87.3	76.6
Echo train length	22	26	100
Scan time, s	332.6	229.1	259.0
Scan orientation	Axial	axial	sagittal

* Pixel bandwidth × rows.

† Reconstruction diameter/acquisition matrix.

‡ Reconstruction diameter/rows.

[Open table in a new tab](#)

From the point of view of tissue contrast, no significant differences were found between the tested sequences. However, 2-dimensional sequences are more sensitive to patient motion (swallowing, eye movements); thus, imaging artifacts are more likely to occur. This is the main reason why the volunteer scan included in the atlas is a 3-dimensional Sagittal T2-weighted sequence, although our contouring atlas is applicable to any diagnostic T2-weighted



sequence. The reconstruction diameter was 350 mm, the pixel size 0.664 mm, and the spacing between slices 0.5 mm. The selection criteria for the atlas case included high resolution, good contrast, and lack of imaging artifacts. Before manual contouring, the original scan was reformatted to axial orientation and isotropic voxel size (0.664 mm) using the Volume Viewer application of Advantage Workstation, version 4.7, to make the scan compatible with all RT planning software



was evaluated on T1- and T2-weighted MRI sequences, as well as on CT. The most important aspects of evaluation were sharpness of margins and demarcation from the surrounding tissues. A scale ranging from 1 to 3 was used, where 3 stood for excellent, 2 for average, and 1 for poor visibility. Based on the results of this evaluation, we found that T2-weighted MRI sequences are more suitable for OAR delineation than T1 sequences. In addition to organ contouring, MRI-only RT planning requires synthetic CT to enable dose calculation. The technical feasibility of MRI-based synthetic CT was demonstrated previously by several studies.^{15,16}

Results

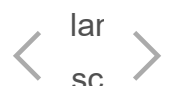
Herein, we summarize our findings during the contouring session, as well as the recommended OAR boundaries. [Table 6](#) also contains useful information on the MRI characteristics of the different OARs by the end of this section.

Parotid glands

The parotid gland is the largest of the major salivary glands, approximately 55 to 60 mm in craniocaudal and 30 to 35 mm in anteroposterior dimension.⁸ The parotid gland is composed of an inverted, triangle-shaped, superficial and deep lobe, located behind the ramus of the mandible. A number of important vessels and nerves pass through the gland. The facial nerve pierces its substance in the posteroanterior direction, which can be regarded as the border between the superficial and deep lobes. Deep to the facial nerve passes the external carotid artery to terminate as 2 branches inside the parotid gland (maxillary and superficial temporal arteries). Superficial to the arteries are the superficial temporal and maxillary veins, joining to form the retromandibular vein.

Contouring suggestions

The delineation of the external carotid artery and retromandibular vein was carried out in a few cases to precisely define the medial border of the organ and distinguish between vessels and the styloid process, as well as the muscles arising from the latter. An accessory pair of salivary glands sometimes present alongside the parotid duct, on the outer surface of the masseteric muscle.



that has to be included in the contour. Fatty infiltration/replacement of the secretory tissue may be present in patients of older age, which may make the outline of the organ more difficult to define.¹⁷ This may also arise as a therapeutic side effect of previous irradiation. [Table 2](#) shows the recommended anatomic boundaries.



Organ boundaries	Parotid glands	Submandibular glands
Anterior	Masseteric muscle, mandibular ramus, pterygoid muscles	Posterior margin of mylohyoid muscle, with the deep process spreading above the mylohyoid muscle
Posterior	Sternocleidomastoid muscle and the posterior belly of the digastric muscle	Parapharyngeal space, great vessels of the neck
Medial	Styloid process, styloglossus, stylohyoid, and stylopharyngeal muscles	Superior: lateral surface of hyoglossus and partly mylohyoid muscles Middle: lateral surface of styloglossus and stylohyoid muscles, digastric muscle Inferior: lateral surface of the body of hyoid bone, pharyngeal constrictor muscles
Lateral	Platysma, subcutaneous tissue	Superior: medial surface of medial pterygoid muscle Middle: medial surface of the body of the mandibular bone

[Open table in a new tab](#)

Submandibular glands

The largest portion of the walnut-sized (approximately 27 mm in length; 13-14 mm in width) submandibular gland lies in the submandibular triangle, and usually exceeds the level of the inferior border of the mandibular corpus (ie, cranial border of submandibular triangle).

cranial direction. Inferiorly, this portion of the gland reaches the insertion of the stylohyoid muscle (body and greater horn of hyoid bone) and the intermediate tendon of the digastricus. A tongue-like extension of the gland, often referred to as the deep process, arises from the medial surface of the gland, and spreads above the mylohyoid muscle. The facial artery leads a tortuous path, which passes through the medial part of the organ, and the facial vein is situated on the superficial surface



[Table 2](#) shows the recommended anatomic boundaries.

Mandible

The mandible, or jawbone, consists of a parabolic-shaped body that is connected by a right and left ramus to the rest of the cranium. The 2 rami terminate in the condyles, which form the articular head of the temporomandibular joints.

Contouring suggestions

The alveoli or teeth sockets of the mandibular corpus are still included in the contour, but not the teeth. We omitted the coronoid process from the contour, because its cranial border is hard to define univocally on axial MRI slices, and radiation necrosis affects primarily the body.¹⁸

Supraglottic larynx

The upper part of the larynx is composed of the epiglottis, aryepiglottic folds, false vocal or vestibular cords, arytenoid cartilages, and mucosa coating them. Brouwer et al¹ defined the inferior border of the supraglottis as the cranial edge of arytenoid cartilages. However, this contradicts the fact that the vestibular cords form an integral part of the supraglottic larynx, because their origin and insertion (anterolateral surface of arytenoid cartilage, just above vocal process; angle of thyroid cartilage below attachment of epiglottis) is situated below the apex of the arytenoids. The pyriform sinus belongs to the hypopharynx and is excluded from the contour.

Glottic larynx/glottic area

The glottic larynx is an anatomic subsite of the larynx, below the supraglottis and above the subglottis. The name of the area is derived from the glottis, the gap between the true vocal cords. According to the seventh edition of the American Joint Committee on Cancer staging manual,¹⁹ the glottis contains the true vocal cords, including its anterior and posterior commissures. The overall thickness of the structure is approximately 10 mm in the horizontal plane.

Contouring suggestions



[Table 3](#) shows the recommended anatomic boundaries of the laryngeal structures.

Table 3 Anatomic borders of laryngeal structures and oral cavity

Anterior	Hyoid bone, pre-epiglottic space, thyroid cartilage ¹	Thyroid angle	Inner surface of superior and inferior dental arches
Posterior	Posterior pharyngeal wall	Inner surface of cricoid and arytenoid cartilages	Posterior border of soft palate and uvula, root of the tongue ¹
Medial	NA (lumen of larynx)		NA
Lateral	Inner surface of thyroid cartilage		Inner surface of dental arches, maxilla, and mandible
Cranial	Tip of epiglottis ¹	Caudal boundary of supraglottic larynx (ie, arytenoids)	Mucosa of hard and soft palates
	1-2 slices below the	Clinically, it varies from 0-1 cm below the free level of the true	Anterior: mylohyoid muscle + anterior

[Open table in a new tab](#)

Oral cavity

Opposite to the previously enumerated structures, the oral cavity is not an organ on its own, but an anatomic area within the mouth that is located anterior to the oropharynx.²⁰ Its contour includes the hard and soft palates, as well as the lingual tonsils, because their mucosa must be spared from an excessive dose of ionizing radiation. This consideration led us to an OAR contour that is somewhat larger than the oral cavity proper (ie, cavity behind dental arches, excluding oral vestibule between lips and teeth).

Contouring suggestions

[Table 3](#) shows the recommended anatomic boundaries.

Pharyngeal constrictor muscles

The muscles of the pharynx can be divided into an outer circular and inner longitudinal layer. The



Contouring suggestions

Apart from the pharyngeal constrictor muscles, various other structures play an indispensable role in the process of swallowing. These structures are the muscles of the floor of the mouth (anterior belly of digastric muscle, mylohyoid and geniohyoid muscle), thyrohyoid muscle, posterior digastric/stylohyoid muscle complex, longitudinal pair of the pharyngeal constrictors (ie, longitudinal pharyngeal muscles), hyoglossus/styloglossus complex, genioglossus muscle, and muscles responsible for tongue motion (intrinsic tongue muscles, referred to collectively as functional swallowing units [FSUs]).^{9,21}

The 3 major physiological roles of these structures are tongue motion, tongue base retraction, and hyolaryngeal elevation. The usefulness of FSU delineation in daily routine is a source of debate due to the extreme workload demand and eventual overlaps with other sensitive areas, such as the oral cavity and certain laryngeal structures. The contouring process might be facilitated in some cases by the usage of automatic OAR segmentation, as stated in the article by the MD Anderson Head and Neck Cancer Symptom Working Group.²² To the best of our knowledge, neither dose constraints nor exact fields of implication have been defined for these structures.

Contouring suggestions

[Table 4](#) shows the recommended anatomic boundaries.

Table 4 Anatomic borders of pharyngeal constrictor muscles



Organ boundaries	Superior pharyngeal constrictor muscle	Middle pharyngeal constrictor muscle	Inferior pharyngeal constrictor muscle
Anterior	Caudal tip of the pterygoid plates ¹³	Hyoid bone, root of the tongue ¹³	Soft tissue of the larynx ¹³



Medial	NA (pharyngeal lumen) ¹³		
Lateral	Medial pterygoid muscle, ¹³ parapharyngeal space	Greater horn of hyoid bone ¹³	Superior horn of thyroid cartilage ^{1,13}
Cranial	Caudal tip of pterygoid plates ^{13,25†}	Cranial edge of C3 vertebra ¹³	First slice caudal to the caudal edge of hyoid bone ¹³
Caudal	Caudal edge of C2 vertebra ¹³	Caudal edge of hyoid bone ^{13,25}	Caudal edge of arytenoid cartilages ¹³

* The former muscle stretches between the base of the skull (insertion: basilar part of occipital bone) and the upper cervical vertebrae (origin: transverse processes of third to sixth cervical vertebrae). The latter lies beneath the longus capitis muscle, on the anterior surface of vertebral bodies, and can be followed all the way down to the level of the upper thoracic vertebrae (origin: bodies of C5-Th3 vertebrae; insertion: anterior arch of the atlas).

† The pterygopharyngeal part of the superior pharyngeal constrictor muscle originates from the lower third of the medial pterygoid plate and its hamulus. Finding the pterygoid process on magnetic resonance images may be challenging; therefore, computed tomography correlation is advisable.

[Open table in a new tab](#)

Inner ear

The inner ear is composed of 2 main functional parts (cochlea and vestibular system), which consist of an outer bony labyrinth, a network of passages with bony walls within the petrous part of the temporal bone, and an inner fluid-filled membranous labyrinth. The cochlea is a spiraled tunnel that makes 2.75 turns about its axis, the modiolus (perpendicular to longitudinal axis of petrous bone). The semicircular canals are situated posterolaterally to the cochlea, of 3 tubes according to the 3 main planes of space, interconnected by a central ves

Contouring suggestions

The cochlea and vestibular system have been delineated separately in some cases. However, due to the proximity of the 2 structures, we defined the inner ear as 1 single OAR, per the practice of Sun et al.²⁷

Eye (evehall)



eye itself, which can be subdivided into 4 further anatomic structures (anterior and posterior chambers, lens, and vitreous body). However, finer microscopic anatomic details cannot be observed on MRI scans.

Contouring suggestions

A meticulous delineation of the fluid filling the anterior chamber and vitreous body can be carried out. The extension of this contour by 1 mm (corresponding to outer layers of the eye) in all dimensions may also lead to an adequate OAR contour.

Lens

The lens of the eye is a biconvex, lentiform structure suspended between the iris and vitreous body. Its overall diameter typically ranges between 9 and 10 mm, with a thickness of approximately 4.5 mm, although this varies with age.

Optic nerve

Also known as cranial nerve II, the optic nerve is composed of ganglion cell axons that carry the excitation of retinal photoreceptors to the vision centers of the cortex. The orbital portion of the nerve is usually between 20 and 30 mm in length and 2 to 5 mm in thickness. The optic nerve travels in the axis of the orbit, above the rectus inferior muscle, and below the rectus superior, and enters the cranial cavity via the optic canal to end in the optic chiasm. The intracranial segment of the optic nerve is approximately 10 mm long.

Contouring suggestions

The optic nerve can be confused with the rectus superior and inferior muscles. The muscles have a flat, shorter appearance, and the nerve is slimmer and longer. The meningeal layers unsheathing the nerve have also been included in the contour.

Optic chiasm

The optic chiasm is the location of the partial decussation of optic fibers, and rests on the tuberculum sellae in the suprasellar cistern. The crossing fibers form an x-shape, p



bordered by the pituitary stalk, laterally by the internal carotid arteries, and inferiorly by the third ventricle. The circle of Willis encircles the pituitary stalk and optic chiasm. The overall size of the structure is usually $14 \times 8 \times 5$ mm.¹⁰

Contouring suggestions

The Y-shape is not always visible on 1 single section, especially when operating with small slice



axons forming the optic tract can be delineated on consecutive MRI slices. The pituitary stalk and internal carotid arteries may be delineated additionally to help distinguish between the chiasm and the surrounding structures.

Lacrimal gland

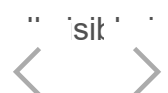
The lacrimal gland is a small exocrine gland situated in a shallow depression of the superolateral corner of the orbit.

Contouring suggestions

The easiest way to find the lacrimal gland is to look for an approximate $15 \times 20 \times 5$ -mm area with low signal intensity above the lateral rectus muscle and laterally to the superior rectus muscle.²⁸ The volume of the lacrimal gland is usually around 0.6 cm^3 with slight right-sided dominance.^{29,30}

Brain stem

The rostral continuation of the spinal cord can be divided into 3 levels in rostrocaudal order. The lowermost one-third, the medulla oblongata, has no well-determined inferior border, because transition from the spinal cord to the brain stem is continuous. To overcome this uncertainty, we commenced the contouring of the medulla at the level where the tip of the odontoid process first appears in concordance with CT-based guidelines.¹ The rostral limit of the mesencephalon, or midbrain (uppermost third of brain stem) is similarly ill-defined. A recent study on OAR contouring in the central nervous system using MRI technique suggested the delineation of the midbrain until the nigral substance disappeared.¹⁰ The previously mentioned CT-based consensus guideline defines the cranial beginning of the midbrain as the bottom section of the lateral ventricles. We do not entirely agree with this approach, because the temporal horns of the lateral ventricles appear already at the level of the pontomesencephalic junction and therefore, more caudally than the expected organ margin. We found that the central part of the lateral ventricle is a more reliable landmark for the upper border of the mesencephalon. Another study by Beddok et al¹¹ suggested placing the brain stem between the upper- and lowermost endpoints of the Sylvian aqueduct, a cerebrospinal fluid-filled narrow cavity that is the sagittal plane.



Contouring suggestions

The average volume of the brain stem is expected to fall between 27 and 43 cm³.³¹

Spinal cord

The spinal cord is the caudal continuation of the brain stem, extending from the lowermost



Brain

The brain contour includes the brain stem, diencephalon, cerebellum, hemispheres of the telencephalon, smaller cerebral vessels, and cerebrospinal fluid. Our approach treats the brain stem as a subunit of the OAR brain; therefore, the lowermost section of these 2 is located in an identical plane.

Contouring suggestions

The contouring of this organ mainly involves following the outline of the cerebrospinal fluid in the subarachnoid space.

Pituitary gland

The pituitary gland, or hypophysis, is a cherry-sized endocrine organ located within the cranial cavity. This gland can be regarded as a caudal protrusion of the hypothalamus, connected by the pituitary stalk to the latter.

Contouring suggestions

The hypophysis rests in a small, saddle-shaped, bony nest of the sphenoid bone, the sella turcica. The organ itself is usually well visible on any diagnostic T2-weighted MRI sequences, although the sella itself is difficult to find. On CT scans with an appropriate bone window, the clinoid processes, dorsum and tuberculum sellae, important anatomic landmarks bordering the hypophyseal fossa, and thus, hypophysis, can be localized.

Thyroid gland

The thyroid gland is an endocrine organ that lies against and around the thyroid and cricoid cartilages of the larynx. This gland is made up of 2 elongated lobes interconnected by a narrow isthmus, giving the thyroids the shape of a butterfly. The size of the lobes may vary on a wide range, but the average anteroposterior diameter of the organ usually falls between 13 and 28 mms, with a length of 40 to 60 mm. The volume of the OAR is 12 to 18 mL in the male and 10 to 15 mL in the female population.^{32,33}



Brachial plexus

The brachial plexus is a network of nerves that provides sensory and motor innervation of the upper limb and shoulder girth. The course of the plexus can be divided into 4 distinct portions, each related to characteristic anatomic landmarks. The first portion (ie, radices or roots of brachial plexus correspond to anterior rami of C5-T1 spinal nerves). These roots later merge to



The last portion of the brachial plexus are cords, located below the clavicle, in the axillary fossa, and are named by their position with respect to the axillary artery.

Contouring suggestions

The recommended anatomic boundaries for the brachial plexus are included in [Table 5](#).

Table 5 Anatomic borders of brachial plexus

Roots	Trunks	Divisions	Cords
First, the intervertebral foramina between C ₄ -C ₅ and T ₁ -T ₂ should be identified. ^{14,34} Of note, cervical spinal nerves emerge above their corresponding vertebrae,* which is why the fifth cervical spinal nerve is found above the fourth cervical vertebra.	The next step is delineating the trunks of the brachial plexus in the scalene hiatus. ^{14,34} The anterior and middle scalene muscles may also be contoured to better understand anatomic relations.	The last 2 portions of the brachial plexus are defined as the posterior part of the subclavian and axillary neurovascular bundle, below the insertion of the middle scalene muscle and the sternal extremity of the clavicle. ^{14,35} A 5-mm paint tool thickness is recommended for the delineation of the organ at risk. ^{34,35} Furthermore, Van der Velde et al suggested adding a margin of 4.7 mm around this brachial plexus contour to achieve full coverage of organ-at-risk and anatomic variants. ³⁶	

* Unlike the rest of the spinal nerves that leave the spinal canal below their corresponding vertebrae.

[Open table in a new tab](#)

Table 6 Comparison between T1- and T2-weighted MRI sequences and CT



Organ	T1w	T2w	CT	Remarks
Parotid glands	2	3	2	Any diagnostic T2w MRI sequence is eligible for delineation purposes because the saliva content of the glands
Submandibular glands	2	3	2	Similar MRI morphology to the parotid glands
Mandible	2	2	3	Contouring the mandible on CT is easier owing to the sharp contrast between the hyperdense bone and the surrounding soft tissues. On T2w MRI, the cortical bone appears as a low signal intensity layer enveloping the inhomogeneous spongy bone
Supraglottic larynx	2	2	2	



Abbreviations: CT = computed tomography; MRI = magnetic resonance imaging.

Visibility of organs is graded from 1 to 3, with 3 = excellent, 2 = average, and 1 = poor visibility.

[Open table in a new tab](#)

Esophagus

Starting at the level of the sixth cervical vertebra, the thumb-thick food pipe interconnects the pharynx with the cardia of the stomach, and rests on the vertebral bodies, just behind the larynx and trachea.

Contouring suggestions

Between the ventral trachea and dorsal esophagus runs the shallow tracheoesophageal groove, which contains the recurrent laryngeal nerve. The sparing of this nerve may be des



prevent late-onset radiation-induced neuropathy.^{37,38}

Discussion

The role of novel anatomic structures and subsites as potential OARs emerges, just as we have



built, straightforward contouring guidelines^{46,47} is on the rise. Automated OAR segmentation (not only in the H&N region), combined with MRI-based imaging, may lead to increased accuracy in terms of organ boundaries and decreased interobserver variability.^{48,49} Generally speaking, the rapid evolution of artificial intelligence–based contouring software may take a huge burden off the shoulders of radiographers and radiation oncologists, and may result in the expansion of this proposed organ set. OAR delineation should always be governed by clinical rationality that takes into account disease stage, tumor volume, and involvement/infiltration of different anatomic structures, functional units, as well as the curative or palliative intent of the radiation therapy itself.

Conclusion

Within the framework of cooperation between several European clinical centers, a consensus guideline was established on OAR delineation in the H&N region, using exclusively magnetic resonance images. Such uniform guidelines may increase treatment accuracy and facilitate the comparison of results between different centers, collaborations, and multi-institutional clinical trials.

Appendix. Supplementary materials



[Download .pdf \(12.17 MB\)](#)

[Help with pdf files](#)

References



1. Brouwer CL • Steenbakkers RJHM • Bourhis J • et al.
CT-based delineation of organs at risk in the head and neck region: DAHANCA, EORTC, GORTEC, HKNPCSG, NCIC CTG, NCRI, NRG Oncology and TROG consensus guidelines.
Radiother Oncol. 2015; **117**: 83-90



2. Widmann G • Henninger B • Kremser C • Jaschke W.
MRI sequences in head & neck radiology—State of the art.
Rofo. 2017; **189**: 413-422

[View in Article](#) ^

[Scopus \(29\)](#) • [PubMed](#) • [Crossref](#) • [Google Scholar](#)

3. Dai YL • King AD.
State of the art MRI in head and neck cancer.
Clin Radiol. 2018; **73**: 45-59

[View in Article](#) ^

[Scopus \(42\)](#) • [PubMed](#) • [Abstract](#) • [Full Text](#) • [Full Text PDF](#) • [Google Scholar](#)

4. Lukovic J • Henke L • Gani C • et al.
MRI-based upper abdominal organs-at-risk atlas for radiation oncology.
Int J Radiat Oncol Biol Phys. 2020; **106**: 743-753

[View in Article](#) ^

[Scopus \(11\)](#) • [PubMed](#) • [Abstract](#) • [Full Text](#) • [Full Text PDF](#) • [Google Scholar](#)

5. Olsson Nyholm T • Wieslander E • et al.
Initial experience with introducing national guidelines for CT- and MRI-based delineation of organs at risk in radiotherapy.
Phys Imaging Radiat Oncol. 2019; **11**: 88-91

[View in Article](#) ^

[Scopus \(3\)](#) • [PubMed](#) • [Abstract](#) • [Full Text](#) • [Full Text PDF](#) • [Google Scholar](#)



6. Yuan J • Wong O • Law MWK • Ding Y • Cheung KY • Yu SK.
Delineation variability of head and neck organs at risk on T1-weighted isotropic magnetic resonance images: A pilot study on healthy volunteers.
Int J Radiat Oncol Biol Phys. 2019; **96**: E609

[View in Article](#) ^



7. Rusko L • Kolozsvari B • Takacs P • et al.
Automated organ delineation in T2 head MRI using combined 2D and 3D convolutional neural networks.
ESTRO. 2020; **0100** (PO-): 1709

[View in Article](#) ^

[Google Scholar](#)

8. Hoebbers F • Yu E • Eisbruch A • et al.
A pragmatic contouring guideline for salivary gland structures in head and neck radiation oncology: The MOIST target.
Am J Clin Oncol. 2013; **36**: 70-76

[View in Article](#) ^

[Scopus \(11\)](#) • [PubMed](#) • [Crossref](#) • [Google Scholar](#)

9. Gawryszuk A • Bijl HP • Holwerda M • et al.
Functional swallowing units (FSUs) as organs-at-risk for radiotherapy. PART 2: Advanced delineation guidelines for FSUs.
Radiother Oncol. 2019; **130**: 68-74

[View in Article](#) ^

[Scopus \(3\)](#) • [PubMed](#) • [Abstract](#) • [Full Text](#) • [Full Text PDF](#) • [Google Scholar](#)

10. Eekers DBP • in 't Ven L • Roelofs E • et al.
The EPTN consensus-based atlas for CT- and MR-based contouring in neuro-oncology.
Radiother Oncol. 2018; **128**: 37-43

[View in Article](#) ^



[Scopus \(49\)](#) • [PubMed](#) • [Abstract](#) • [Full Text](#) • [Full Text PDF](#) • [Google Scholar](#)

11. Beddok A • Faivre JC • Coutte A • et al.

Practical contouring guidelines with an MR-based atlas of brainstem structures involved in radiation-induced nausea and vomiting.



[Scopus \(5\)](#) • [PubMed](#) • [Abstract](#) • [Full Text](#) • [Full Text PDF](#) • [Google Scholar](#)

12. Wu AJ • Bosch WR • Chang DT • et al.

Expert consensus contouring guidelines for IMRT in esophageal and gastroesophageal junction cancer.

Int J Radiat Oncol Biol Phys. 2015; **92**: 911-920

[View in Article](#) ^

[Scopus \(82\)](#) • [PubMed](#) • [Abstract](#) • [Full Text](#) • [Full Text PDF](#) • [Google Scholar](#)

13. Christianen MEMC • Langendijk JA • Westerlaan HE • van de Water TA • Bijl HP.
Delineation of organs at risk involved in swallowing for radiotherapy treatment planning.

Radiother Oncol. 2011; **101**: 394-402

[View in Article](#) ^

[Scopus \(130\)](#) • [PubMed](#) • [Abstract](#) • [Full Text](#) • [Full Text PDF](#) • [Google Scholar](#)

14. Truong MT • Nadgir RN • Hirsch AE • et al.

Brachial plexus contouring with CT and MR imaging in radiation therapy planning for head and neck cancer.

Radiographics. 2010; **30**: 1095-1103

[View in Article](#) ^

[Scopus \(30\)](#) • [PubMed](#) • [Crossref](#) • [Google Scholar](#)

15. Wiesinger F • Bylund M • Yang J • et al.

Zero TE-based pseudo-CT image conversion in the head and its application in PET/MR attenuation correction and MR-guided radiation therapy planning

Magn Reson Med. 2018; **80**: 1440-1451



[View in Article](#) ^

[Scopus \(62\)](#) • [PubMed](#) • [Crossref](#) • [Google Scholar](#)

16. Blanc-Durand P • Khalife M • Sgard B • et al.

Attenuation correction using 3D deep convolutional neural network for brain 18F-FDG



[View in Article](#) ^

[Scopus \(25\)](#) • [PubMed](#) • [Crossref](#) • [Google Scholar](#)

17. Sousa Garcia D • Bussoloti Filho I

Fat deposition of parotid glands.

Braz J Otorhinolaryngol. 2013; **79**: 173-176

[View in Article](#) ^

[Scopus \(9\)](#) • [PubMed](#) • [Crossref](#) • [Google Scholar](#)

18. Rathy R • Sunil S • Nivia M.

Osteoradionecrosis of mandible: Case report with review of literature.

Contemp Clin Dent. 2013; **4**: 251-253

[View in Article](#) ^

[Scopus \(11\)](#) • [PubMed](#) • [Crossref](#) • [Google Scholar](#)

19. Edge SB • Byrd DR • Compton CC • Fritz AG • Greene FL

AJCC Cancer Staging Manual Seventh Edition.

(Trotti A III, eds) Springer, New York, NY2010

[View in Article](#) ^

[Google Scholar](#)

20. Williams 3rd, DW

An imager's guide to normal neck anatomy.

Semin Ultrasound CT MR. 1997; **18**: 157-181

[View in Article](#) ^

[Scopus \(17\)](#) • [PubMed](#) • [Crossref](#) • [Google Scholar](#)



21. Gawryszuk A • Bijl HP • Holwerda M • et al.
Functional swallowing units (FSUs) as organs-at-risk for radiotherapy. PART 1: Physiology and anatomy.
Radiother Oncol. 2019; **130**: 62-67

[View in Article](#) ^



22. MD Anderson Head and Neck Cancer Symptom Working Group
Beyond mean pharyngeal constrictor dose for beam path toxicity in non-target swallowing muscles: Dose-volume correlates of chronic radiation-associated dysphagia (RAD) after oropharyngeal intensity modulated radiotherapy.
Radiother Oncol. 2016; **118**: 304-314

[View in Article](#) ^

[Scopus \(66\)](#) • [PubMed](#) • [Abstract](#) • [Full Text](#) • [Full Text PDF](#) • [Google Scholar](#)

23. Ferlito A • Rinaldo A.
The pathology and management of subglottic cancer.
Eur Arch Otorhinolaryngol. 2000; **257**: 168-173

[View in Article](#) ^

[Scopus \(32\)](#) • [PubMed](#) • [Crossref](#) • [Google Scholar](#)

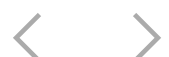
24. Dirix P • Abbeel S • Vanstraelen B • Hermans R • Nuyts S.
Dysphagia after chemoradiotherapy for head-and-neck squamous cell carcinoma: Dose-effect relationships for the swallowing structures.
Int J Radiat Oncol Biol Phys. 2009; **75**: 385-392

[View in Article](#) ^

[Scopus \(142\)](#) • [PubMed](#) • [Abstract](#) • [Full Text](#) • [Full Text PDF](#) • [Google Scholar](#)

25. Popovtzer A • Cao Y • Feng FY • Eisbruch A.
Anatomical changes in the pharyngeal constrictors after chemoradiation of head and neck cancer and their dose-effect relationships: MRI-based study.
Radiother Oncol. 2009; **93**: 510-515

[View in Article](#) ^



[Scopus \(73\)](#) • [PubMed](#) • [Abstract](#) • [Full Text](#) • [Full Text PDF](#) • [Google Scholar](#)

26. Bhandare N • Jackson A • Eisbruch A • et al.

Radiation therapy and hearing loss.

Int J Radiat Oncol Biol Phys. 2010; **76**: S50-S57



[Scopus \(73\)](#) • [PubMed](#) • [Abstract](#) • [Full Text](#) • [Full Text PDF](#) • [Google Scholar](#)

27. Sun Y • Yu XL • Luo W • et al.

Recommendation for a contouring method and atlas of organs at risk in nasopharyngeal carcinoma patients receiving intensity-modulated radiotherapy.

Radiother Oncol. 2014; **110**: 390-397

[View in Article](#) ^

[Scopus \(98\)](#) • [PubMed](#) • [Abstract](#) • [Full Text](#) • [Full Text PDF](#) • [Google Scholar](#)

28. Scoccianti S • Detti B • Gadda D • et al.

Organs at risk in the brain and their dose-constraints in adults and in children: A radiation oncologist's guide for delineation in everyday practice.

Radiother Oncol. 2015; **114**: 230-238

[View in Article](#) ^

[Scopus \(124\)](#) • [PubMed](#) • [Abstract](#) • [Full Text](#) • [Full Text PDF](#) • [Google Scholar](#)

29. Bulbul E • Yazici A • Yanik B • Yazici H • Demirpolat G.

Evaluation of lacrimal gland dimensions and volume in Turkish population with computed tomography.

J Clin Diagn Res. 2016; **10**: TC06-TC08

[View in Article](#) ^

[PubMed](#) • [Google Scholar](#)

30. Totuk OMG • Kalkay AB • Kabadayi K • Demir MK • Barut C.

Evaluation of lacrimal gland dimensions with MR imaging in a Turkish population sample.

Int J Morphol. 2018; **36**: 1431-1438



[View in Article](#) 

[Scopus \(1\)](#) • [Crossref](#) • [Google Scholar](#)

31. Mayo C • Yorke E • Merchant TE.
Radiation associated brainstem injury.



[View in Article](#) 

[Scopus \(223\)](#) • [PubMed](#) • [Abstract](#) • [Full Text](#) • [Full Text PDF](#) • [Google Scholar](#)

32. Chaudhary V • Bano S
Thyroid ultrasound.
Indian J Endocrinol Metab. 2013; **17**: 219-227

[View in Article](#) 

[PubMed](#) • [Crossref](#) • [Google Scholar](#)

33. Kang T • Kim DW • Lee YJ • et al.
Magnetic resonance imaging features of normal thyroid parenchyma and incidental diffuse thyroid disease: A single-center study.
Front Endocrinol (Lausanne). 2018; **9**: 746

[View in Article](#) 

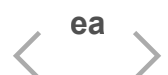
[Scopus \(2\)](#) • [PubMed](#) • [Crossref](#) • [Google Scholar](#)

34. Hall WH • Guiou M • Lee NY • et al.
Development and validation of a standardized method for contouring the brachial plexus: Preliminary dosimetric analysis among patients treated with IMRT for head-and-neck cancer.
Int J Radiat Oncol Biol Phys. 2008; **72**: 1362-1367

[View in Article](#) 

[Scopus \(101\)](#) • [PubMed](#) • [Abstract](#) • [Full Text](#) • [Full Text PDF](#) • [Google Scholar](#)

35. Yi SK • Hall WH • Mathai M • et al.
Validating the RTOG-endorsed brachial plexus contouring atlas: An evaluation of reproducibility among patients treated by intensity modulated radiotherapy and-neck cancer.



Int J Radiat Oncol Biol Phys. 2012; **82**: 1060-1064

[View in Article](#) ^

[Scopus \(23\)](#) • [PubMed](#) • [Abstract](#) • [Full Text](#) • [Full Text PDF](#) • [Google Scholar](#)

36. Van de Velde JI • Audenaert F • Sneleers R • et al



~~Radiation therapy planning.~~

Int J Radiat Oncol Biol Phys. 2013; **87**: 802-808

[View in Article](#) ^

[Scopus \(22\)](#) • [PubMed](#) • [Abstract](#) • [Full Text](#) • [Full Text PDF](#) • [Google Scholar](#)

37. Shultz DB • Trakul N • Maxim PG • Diehn M • Loo Jr., BW

Vagal and recurrent laryngeal neuropathy following stereotactic radiation therapy in the chest.

Pract Radiat Oncol. 2014; **4**: 272-278

[View in Article](#) ^

[Scopus \(13\)](#) • [PubMed](#) • [Abstract](#) • [Full Text](#) • [Full Text PDF](#) • [Google Scholar](#)

38. Jaruchinda P • Jindavijak S • Singhavarach N.

Radiation-related vocal fold palsy in patients with head and neck carcinoma.

J Med Assoc Thai. 2012; **95**: S23-S28

[View in Article](#) ^

[PubMed](#) • [Google Scholar](#)

39. Castelijns JA • Doornbos J • Verbeeten Jr, B • Vielvoye GJ • Bloem JL.

MR imaging of the normal larynx.

J Comput Assist Tomogr. 1985; **9**: 919-925

[View in Article](#) ^

[Scopus \(34\)](#) • [PubMed](#) • [Crossref](#) • [Google Scholar](#)

40. Dean JA • Welsh LC • Gulliford SL • Harrington KJ • Nutting CM.

A novel method for delineation of oral mucosa for radiotherapy dose-response studies.



Radiother Oncol. 2015; **115**: 63-66

[View in Article](#) ^

[Scopus \(19\)](#) • [PubMed](#) • [Abstract](#) • [Full Text](#) • [Full Text PDF](#) • [Google Scholar](#)

41 Adachi M • Hosoya T • Haku T • Yamaguchi K • Kawanami T



accomplished using magnetic resonance weighted mr imaging.

AJNR Am J Neuroradiol. 1999; **20**: 1500-1506

[View in Article](#) ^

[PubMed](#) • [Google Scholar](#)

42. Wada M • Premoselli L • Rolfo A • et al.

Determination of accuracy in the delineation of spinal cord and canal/theal sac on CT and MRI in head and neck planning.

Int J Radiat Oncol Biol Phys. 2006; **66**: S450

[View in Article](#) ^

[Abstract](#) • [Full Text](#) • [Full Text PDF](#) • [Google Scholar](#)

43. Combs SE • Baumert BG • Bendszus M • et al.

ESTRO ACROP guideline for target volume delineation of skull base tumors.

Radiother Oncol. 2021; **156**: 80-94

[View in Article](#) ^

[Scopus \(12\)](#) • [PubMed](#) • [Abstract](#) • [Full Text](#) • [Full Text PDF](#) • [Google Scholar](#)

44. Zhang X • Chen H • Chen W • et al.

Technical note: Atlas-based auto-segmentation of masticatory muscles for head and neck cancer radiotherapy.

J Appl Clin Med Phys. 2020; **21**: 233-240

[View in Article](#) ^

[Scopus \(2\)](#) • [PubMed](#) • [Crossref](#) • [Google Scholar](#)

45. Valstar MH • de Bakker BS • Steenbakkens RJHM • et al.

The tubarial salivary glands: A potential new organ at risk for radiotherap



Radiother Oncol. 2021; **154**: 292-298

[View in Article](#) ^

[Scopus \(40\)](#) • [PubMed](#) • [Abstract](#) • [Full Text](#) • [Full Text PDF](#) • [Google Scholar](#)

46. Grégoire V • Evans M • Le QT • et al



hypopharyngeal, oropharyngeal and oral cavity squamous cell carcinoma: ARCO, CACA, DAHANCA, EORTC, GEORCC, GORTEC, HKNPCSG, HNCIG, IAG-KHT, LPRHHT, NCIC CTG, NCRI, NRG Oncology, PHNS, SBRT, SOMERA, SRO, SSHNO, TROG consensus guidelines.

Radiother Oncol. 2018; **126**: 3-24

[View in Article](#) ^

[Scopus \(173\)](#) • [PubMed](#) • [Abstract](#) • [Full Text](#) • [Full Text PDF](#) • [Google Scholar](#)

47. Lin D • Lapen K • Sherer MV • et al.

A systematic review of contouring guidelines in radiation oncology: Analysis of frequency, methodology, and delivery of consensus recommendations.

Int J Radiat Oncol Biol Phys. 2020; **107**: 827-835

[View in Article](#) ^

[Scopus \(3\)](#) • [PubMed](#) • [Abstract](#) • [Full Text](#) • [Full Text PDF](#) • [Google Scholar](#)

48. Ayyalusamy A • Vellaiyan S • Subramanian S • et al.

Auto-segmentation of head and neck organs at risk in radiotherapy and its dependence on anatomic similarity.

Radiat Oncol J. 2019; **37**: 134-142

[View in Article](#) ^

[Scopus \(16\)](#) • [PubMed](#) • [Crossref](#) • [Google Scholar](#)

49. Tong N • Gou S • Yang S • Ruan D • Sheng K.

Fully automatic multi-organ segmentation for head and neck cancer radiotherapy using shape representation model constrained fully convolutional neural networks.

Med Phys. 2018; **45**: 4558-4567

[View in Article](#) ^



Article Info

Publication History



Received: April 20, 2022

Publication stage

In Press Journal Pre-Proof

Footnotes

Sources of support: This research is part of the Deep MR-only Radiation Therapy activity (project numbers 19037, 20648, and 210995) that has received funding from EIT Health. EIT Health is supported by the European Institute of Innovation and Technology, a body of the European Union that receives support from the Horizon 2020 Research and innovation program.

Disclosures: Dr Paczona reports financial support was provided by EIT Health.

Data sharing statement: Research data are stored in an institutional repository and will be shared upon request to the corresponding author.

Identification

DOI: <https://doi.org/10.1016/j.adro.2022.101042>

Copyright

© 2022 Published by Elsevier Inc. on behalf of American Society for Radiation Oncology.

User License

[Creative Commons Attribution – NonCommercial – NoDerivs \(CC BY-NC-ND 4.0\)](#) |

[How you can reuse](#) 

ScienceDirect

[Access this article on ScienceDirect](#)

Tables



[Table 1 : Scan parameters for 3 T2-weighted sequences used for organ-at-risk delineation](#)

[Table 2: Anatomic borders of salivary glands](#)

[Table 3: Anatomic borders of laryngeal structures and oral cavity](#)

[Table 4: Anatomic borders of pharyngeal constrictor muscles](#)



[Table 6: Comparison between T1- and T2-weighted MRI sequences and CT](#)

Related Articles

[Interobserver Variability of Gross Tumor Volume Delineation for Colorectal Liver Metastases Using Computed Tomography and Magnetic Resonance Imaging](#)

Marshall et al.

Advances in Radiation Oncology, July 23, 2022

[Preview](#) • [Full-Text](#) • [PDF](#)

[Open Access](#)

[Magnetic Resonance Imaging for Breast Tumor Bed Delineation: Computed Tomography Comparison and Sequence Variation](#)

Lowrey et al.

Advances in Radiation Oncology, May 25, 2021

[Preview](#) • [Full-Text](#) • [PDF](#)

[Open Access](#)

[Robustness and Generalizability of Deep Learning Synthetic Computed Tomography for Positron Emission Tomography/Magnetic Resonance Imaging–Based Radiation Therapy Planning of Patients With Head and Neck Cancer](#)

Olin et al.

Advances in Radiation Oncology, July 25, 2021

[Preview](#) • [Full-Text](#) • [PDF](#)

[Open Access](#)

[Brain Metastasis Incidence and Patterns of Presentation After Definitive Treatment of Locally Advanced Non-Small Cell Lung Cancer: A Potential Argument for Brain Magnetic Resonance Imaging Surveillance](#)



Farris et al.

Advances in Radiation Oncology, October 23, 2022

[Preview](#) • [Full-Text](#) • [PDF](#)

[Open Access](#)



Leeman et al.

Advances in Radiation Oncology, March 6, 2022

[Preview](#) • [Full-Text](#) • [PDF](#)

[Open Access](#)

[Home](#)

[Author
Instructions](#)

[Contact
Information](#)

[Healthcare
Disparities](#)

[The Red Journal](#)

ca

**ARTICLES &
ISSUES**

[Permissions](#)

[Editorial Board](#)

[Immunotherapy](#)

[Submit](#)

[Issue in Progress](#)

[Researcher
Academy](#)

[Editorial Board
COI Disclosures](#)

[Podcasts](#)

**MORE
PERIODICALS**

[Current Issue](#)

[Submit a
Manuscript](#)

[New Content
Alerts](#)

ASTRO

[Find a Periodical](#)

[List of Issues](#)

[ASTRO Online](#)

[Go to Product
Catalog](#)

[Articles In Press](#)

JOURNAL INFO

COLLECTIONS

[ASTRO
Guidelines](#)

FOLLOW US

FOR AUTHORS

[About the Journal](#)

[COVID-19
Scientific](#)

[RT Answers](#)

[Twitter](#)

[About Open
Access](#)

[Advertising
Information](#)

[Communications
and Comments](#)

[PRO](#)

[Facebook](#)

We use cookies to help provide and enhance our service and tailor content. To update your cookie settings, please visit the [Cookie Settings](#) for this site.

Copyright © 2022 Elsevier Inc. except certain content provided by third parties. The content on this site is intended for healthcare professionals.

[Privacy Policy](#) [Terms and Conditions](#) [Accessibility](#) [Help & Contact](#)



